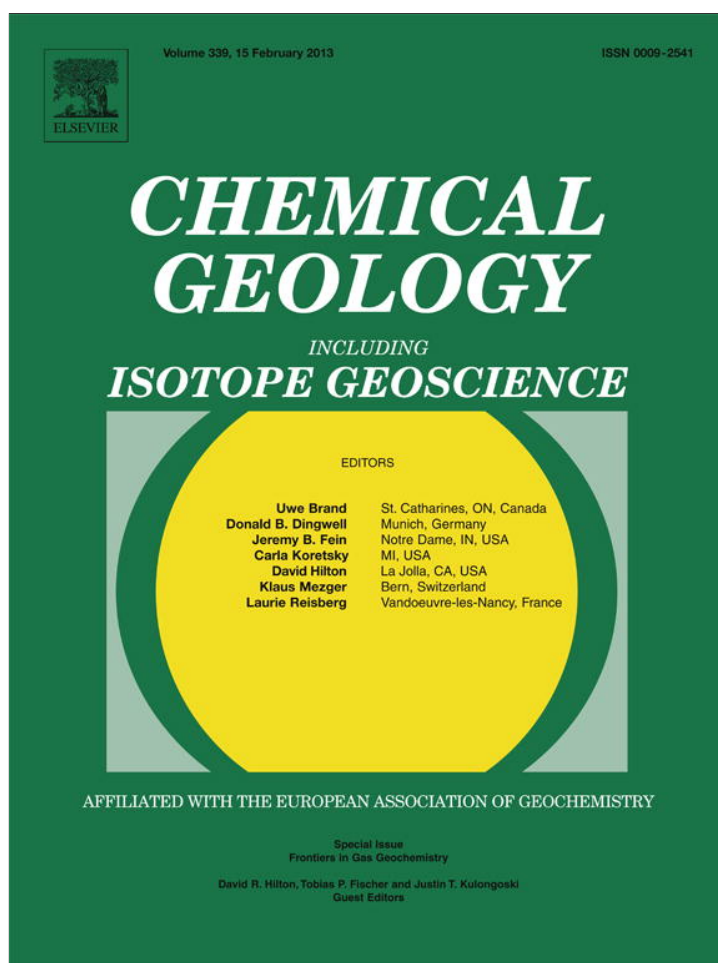


Provided for non-commercial research and education use.  
Not for reproduction, distribution or commercial use.



This article appeared in a journal published by Elsevier. The attached copy is furnished to the author for internal non-commercial research and education use, including for instruction at the authors institution and sharing with colleagues.

Other uses, including reproduction and distribution, or selling or licensing copies, or posting to personal, institutional or third party websites are prohibited.

In most cases authors are permitted to post their version of the article (e.g. in Word or Tex form) to their personal website or institutional repository. Authors requiring further information regarding Elsevier's archiving and manuscript policies are encouraged to visit:

<http://www.elsevier.com/copyright>



Contents lists available at SciVerse ScienceDirect

## Chemical Geology

journal homepage: [www.elsevier.com/locate/chemgeo](http://www.elsevier.com/locate/chemgeo)

# Thermal fluids along the East Anatolian Fault Zone (EAFZ): Geochemical features and relationships with the tectonic setting

Francesco Italiano <sup>a,\*</sup>, Ahmet Sasmaz <sup>b</sup>, Galip Yuce <sup>c</sup>, Ozlem O. Okan <sup>b</sup>

<sup>a</sup> INGV, Istituto Nazionale di Geofisica e Vulcanologia, Palermo, Italy

<sup>b</sup> Firat University, Department of Geology, 23119 Elazığ Turkey

<sup>c</sup> Eskisehir Osmangazi University, Department of Geology, 26480 Eskisehir Turkey

## ARTICLE INFO

## Article history:

Accepted 28 July 2012

Available online 18 August 2012

## Keywords:

Gas geochemistry

Active fault

Fluid/fault relationships

Gas water interactions

## ABSTRACT

A geochemical investigation has been carried out on the gas phase associated to thermal fluids discharged along three different segments of the East Anatolian Fault Zone (EAFZ, Turkey) running from Malatya to the Triple Junction area (Karlöva) where the East and North Anatolian Faults cross each other. CO<sub>2</sub> is always the major gaseous component in both bubbling and dissolved gases with variable amounts of nitrogen helium and CH<sub>4</sub>. The isotopic ratios of helium range from 0.44 to 4.41Rac (values corrected for the atmospheric contamination) and cover a range spanning from crustal to magmatic-type values. The isotopic composition of carbon (CO<sub>2</sub>) shows values in the range from −5.6 to −0.2‰ vs PDB for the bubbling gases in contrast with the positive values (from 0.3 to 3.4‰ vs PDB) detected for the Total Dissolved Inorganic Carbon (TDIC). Coupling the information from the isotopic and chemical compositions, it results that mantle-derived fluids are driven to the surface by lithospheric structures. Despite the absence of outcropping volcanic products, the tectonic setting of the different segments plays a major role in releasing mantle-type fluids. The mantle derived fluids interact at shallower levels with circulating waters and originate geothermal systems which equilibration temperatures are estimated to be up to 360 °C. The collected thermal fluids show different geochemical features consistent with processes occurring at two different levels: a deep level where mantle-originated fluids are taken either from the upper mantle or from intruded magma batches, and a shallower level, in the upper crust, where Gas Water Interactions (GWI), secondary CO<sub>2</sub> production, and fractionation processes induced chemical and isotopic modifications of the pristine gas composition.

© 2012 Elsevier B.V. All rights reserved.

## 1. Introduction

The EAFZ runs in a north-easterly direction, from the northern end of the Dead Sea Transform (Maras Triple Junction) to the Karlöva Triple Junction where it crosses the North Anatolian Fault. The EAFZ is a 580 km-long major strike-slip fault zone forming the transform type tectonic boundary between the Anatolian and the Arabian Plates (Fig. 1). The East and North Anatolian faults together accommodate the westward motion of the Anatolian Plate as it is squeezed out by the ongoing collision with the Eurasian Plate (Fig. 1a). The difference in the relative motions of the two plates is manifested in the left-lateral motion along the EAF which tectonic activity is clearly documented by the seismicity of the entire fault long, the focal depth of the main events as well as by the volcanism of the eastern area.

Along the fault zone, many “harabe” (ruins and deserted villages) testify large earthquakes occurred in the past. Ambraseys (1989) and Ambraseys and Jackson (1998) reported two large historical earthquakes (Fig. 1) on May 3, 1874, and March 27, 1875, on the Palu–Lake Hazar

Segment (PLHS), with estimated magnitudes of >7.1 and 6.7, respectively. The latter earthquake produced an estimated surface rupture of about 20 km with 2 m of vertical offset (Ambraseys, 1989). According to the official records of Ottoman Empire, a catastrophic event occurred near Palu on May 29, 1789 (Fig. 1), destroying settlements in a 75 km-radius area and killing about 51,000 people (Ambraseys, 1989). According to an Ottoman time diary, the towns of Malatya, Adana and Tarsus were almost totally destroyed by an earthquake in 1513, which might be the same earthquake felt in Egypt on March 28, 1513, that caused heavy damages along 340 km of the EAFZ (Ambraseys, 1989). Among the recent seismic events, the M6.8 destructive earthquake of Bingöl in 1971 (Karlöva–Bingöl Segment; 755 casualties) generated a surface rupture of about 35–38 km with maximum left-lateral and vertical offsets of 60 and 10 cm, respectively (Seymen and Aydın, 1972; Arpat and Saroglu, 1972; Keightley, 1975; Ambraseys and Jackson, 1998). A further event (M4.9, March 26, 1977) hit the north-eastern end of the Palu–Lake Hazar Segment (PLHS; Fig. 1b, 8 people killed and 209 dwellings damaged; Ates and Bayulke, 1977; Jackson and McKenzie, 1984). The fault plane solution indicated a left-lateral movement and a focal depth of 25 km (Jackson and McKenzie, 1984; Cetin et al., 2003). The most destructive earthquakes have generally a relatively shallow focal depth, however the seismicity of the EAFZ is characterized by both shallow

\* Corresponding author at: via U. La Malfa 153, Palermo, Italy.

E-mail addresses: [fitaliano@pa.ingv.it](mailto:fitaliano@pa.ingv.it) (F. Italiano), [asasmaz@firat.edu.tr](mailto:asasmaz@firat.edu.tr) (A. Sasmaz), [galipyuce@gmail.com](mailto:galipyuce@gmail.com) (G. Yuce), [oz\\_okan@hotmail.com](mailto:oz_okan@hotmail.com) (O.O. Okan).

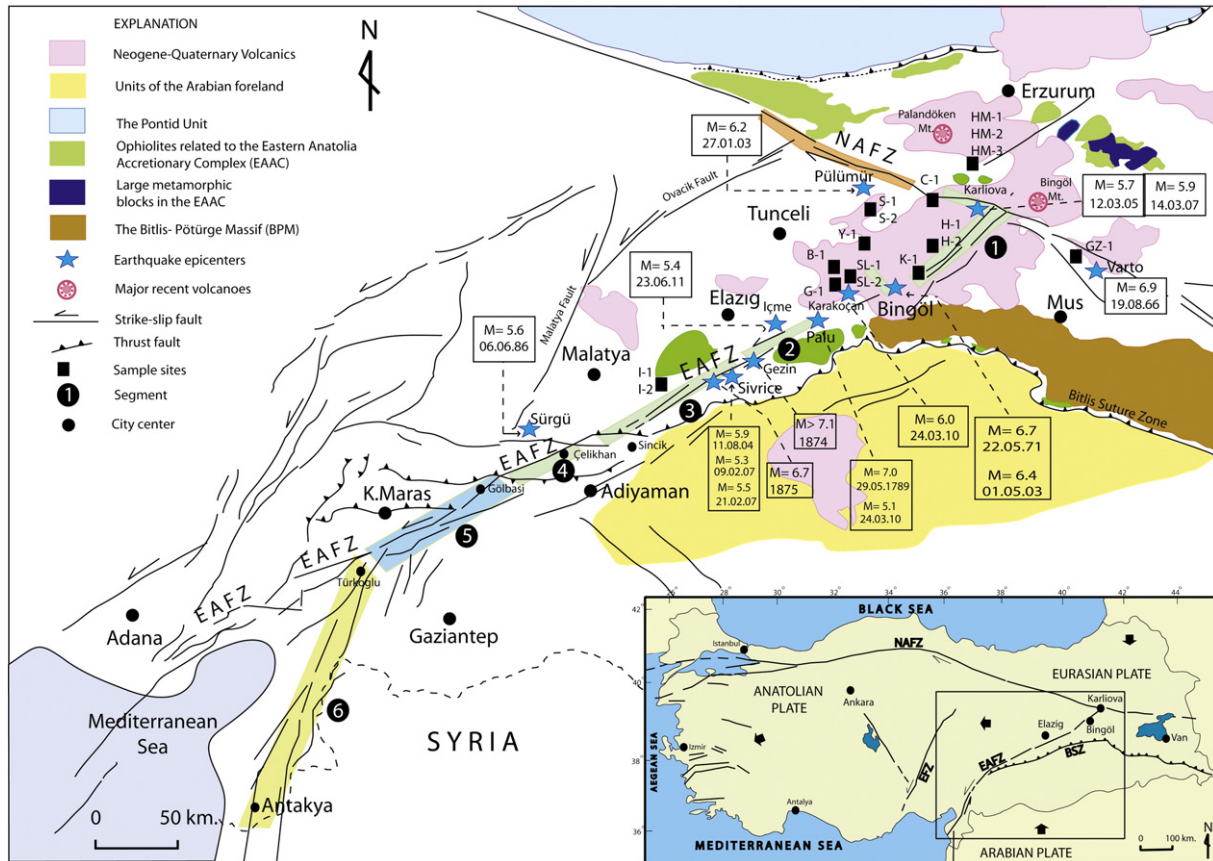


**Fig. 1.** The general map shows the main fault systems in and around Turkey (modified from Barka and Kadinsky-Cade, 1988; Saroglu et al., 1992; Kocyigit and Beyhan, 1998; Okay et al., 2000). The black thick arrows indicate relative plate motions. The detailed map of the EAFZ region displays segments, sampling sites, and the main seismic events (modified from Perincek et al., 1987; Kozlu, 1987; Perincek and Cemen, 1990; Saroglu et al., 1992; Aksu et al., 1992). NAFZ: North Anatolian Fault Zone; EAFZ: East Anatolian Fault Zone; EFZ: Eceemis Fault Zone; BSZ: Bilitis Suture Zone. The black dots indicate the epicentral areas for the shocks detailed in the squared labels with magnitude and date. Squared marks = sampling site labels = collected samples (see Table 1). Black filled circles = EAFZ segments; segment numbers: 1 – Karliova-Bingöl segment; 2 – Palu-Lake Hazar segment; 3 – Lake Hazar-Sincik segment; 4 – Çelikhan-Erkenek segment; 5 – Gölbasi-Türkoglu segment; 6 – Türkoglu-Antakya segment.

(3–10 km) and deep (25–50 km) hypocenters. Deep hypocentral depths denote a lithospheric nature of the fault, which, on the basis of the information about the crustal thickness (between 25 and 40–45 km, Arslan et al., 2010), is able to reach the upper mantle providing a preferential way for mantle fluids to escape.

Mantle-derived/volcanic fluids play an important role along the active tectonic structures in Turkey (e.g. Gulec et al., 2002; de Leeuw et al., 2010) and although volcanic edifices are lacking along the EAFZ, the presence of thermal springs is an indication for volcanic fluid circulation. Thermal fluid venting is known from many different sites although their geochemical features are mostly unknown.

Three segments of this active fault were considered for sampling collection of thermal fluids with the aim to constrain their origin to better understand the relationships between the circulating fluids and the fault activity. Compositional changes of the circulating fluids can be detected during faulting activity as a consequence of modifications in the mixing proportion of volatiles marked by different origin and provenance. Fixing the various components and their origin, and estimating the mixing proportions give valuable information to evaluate the activity and the faulting-induced fluid migration. Samples of both free and dissolved gases were taken from thermal springs displaying outlet temperatures in the range of 17–67 °C.

This paper accounts for the first comprehensive geochemical investigation, including chemical and isotopic compositions (carbon, helium)

of dissolved and bubbling gases, released along the Karliova–Bingöl, Palu–Lake Hazar, and Lake Hazar–Sincik segments of the EAFZ. Three sampling sites were selected over the Karliova triple junction area: two of them are located on the NAFZ (Catak–Erzurum and Guzelkent–Varto) and one more, Hamzan, is located on the possible prosecution of the EAFZ towards North–East (Fig. 1b). Such a geographical distribution covered the whole Karliova triple junction area.

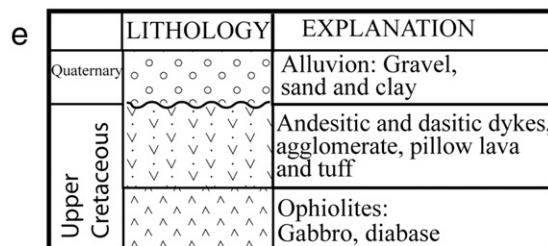
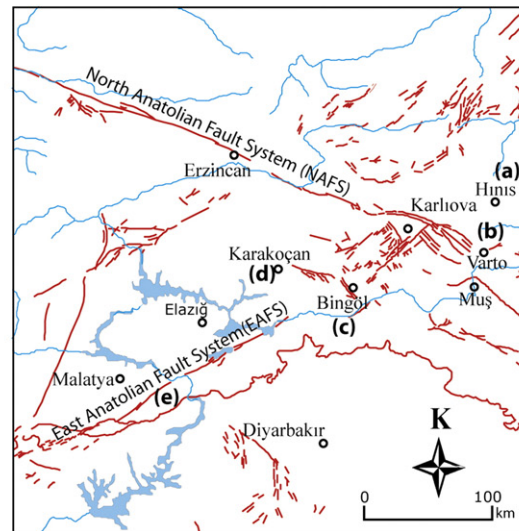
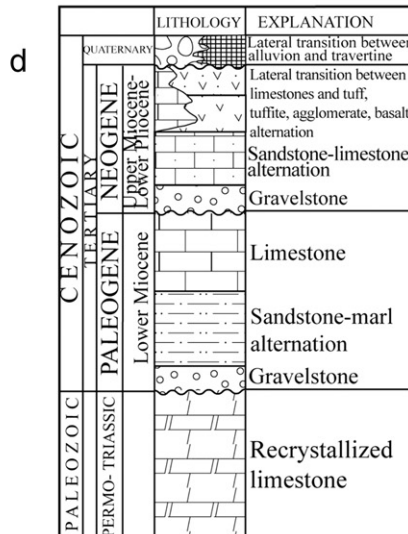
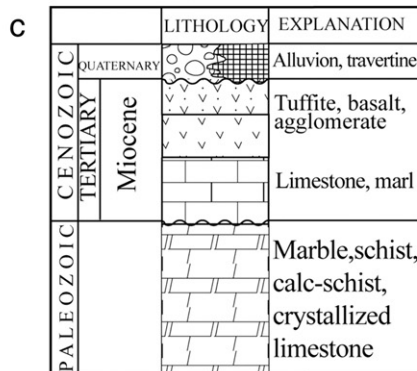
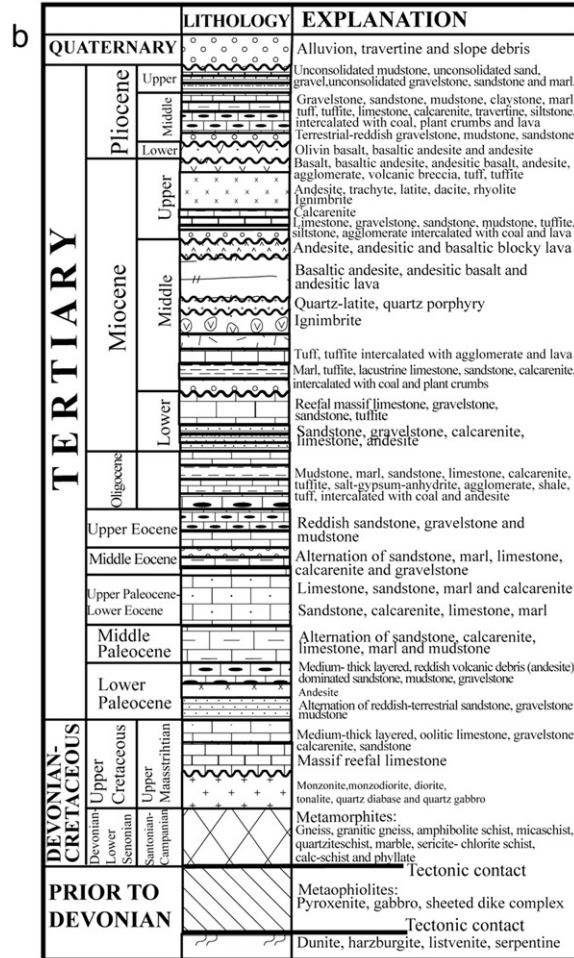
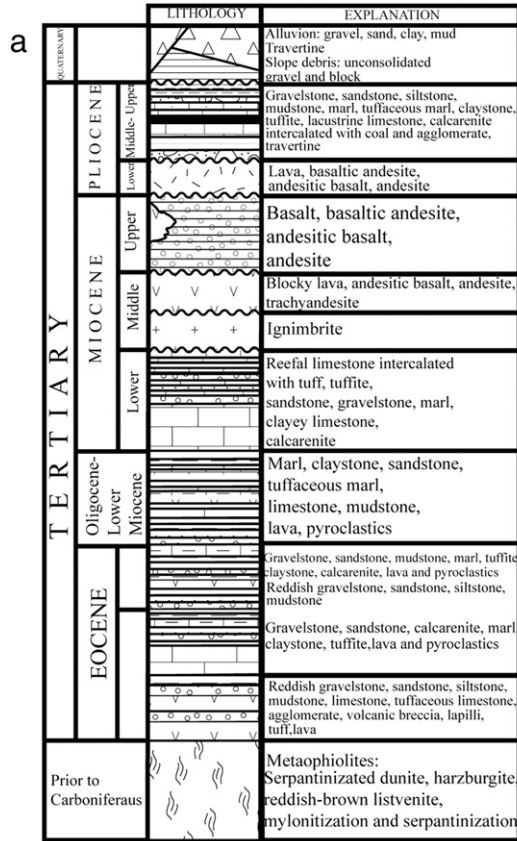
Consistently with previous studies on the North Anatolian Fault Zone (Gulec et al., 2002; de Leeuw et al., 2010), our results show contributions, variable from site to site, of mantle-derived and crustal fluids as well as intense gas–water interactions (GWI), that together with degassing and other processes occurring at relatively shallow depth are responsible for the large variety of geochemical characters of the discharged fluids.

**2. Geologic and tectonic setting**

On the basis of the nature of underlying basement, the Eastern Anatolian contractional zone can be separated into four main crustal terrains: from north to south i) the Pontide Belt, ii) the Eastern Anatolian Accretionary Complex (EAAC), iii) the Bitlis–Pötürge Massif (BPM), and iv) the Arabian Foreland. The Pontide Belt is located in the northern most part of the region. Its basement is represented by a metamorphic massif named the Pulur Complex. The Pulur complex is

**Fig. 2.** Typical geological sections for various East Anatolian Fault Zone (EAFZ) segments. The simplified map in the box shows the location for the stratigraphic sequences of: (a) Tekman–Erzurum (after Taşkıran, 2006); (b) Hinis and Varto (after Tarhan, 1991); (c) Bingöl (after Erisen et al., 1996); (d) Karakocan–Elazığ (after Öztekin Okan and Çetindağ, 2005; Cetindağ et al., 2009); and (e) Ispendere–Malatya (after Cetindağ et al., 1993).





composed of a heterogeneous set of granulite facies rocks, ranging from quartz-rich mesocratic gneisses to silica- and alkali-deficient, Fe-, Mg- and Al-rich melanocratic rocks (Topuz et al., 2004). A thick volcano-sedimentary arc sequence overlies this metamorphic basement.

The EAAC forms a 150–180 km wide, NW-SE extending belt in the middle of the region. It represents the remnant of a huge subduction-accretion complex formed on a north-dipping subduction zone located between the Pontide Belt in the north and the Bitlis–Pötürge microcontinent in the south in a period between the Late Cretaceous and the Oligocene (Sengör et al., 2003). It consists of two contrasting rock units: an ophiolitic melange of Late Cretaceous age, and Paleocene to Late Oligocene flysch sequences incorporated into the ophiolitic melange as north-dipping tectonic slices. This observation is consistent with the polarity of the subduction zone that is thought to have created the Eastern Anatolian accretionary prism by underthrusting.

The Bitlis–Pötürge Massif is exposed in a NW-SE extending belt along the Eastern Taurus mountain range. It is regarded as the easternmost extremity of the Menderes–Taurus block. It consists of medium-to-highly metamorphosed units. Shallow marine deposits of Oligocene to Middle Miocene age unconformably overlie these tectonic blocks in some places (Keskin, 2003). The EAFZ crosses the above mentioned geological units running from Karlıova to Turkoğlu with a total length of about 580 km. The most recent interpretations propose the EAFZ as divided into several distinct geometric segments (Fig. 1b) based on fault stepovers, separations (gaps) or changes in fault strike (Arpat and Saroglu, 1972; Hempton et al., 1981; Sengör et al., 1985; Muehlberger and Gordon, 1987; Westaway, 1994). The segment of the fault physically defined between Lake Hazar and Palu is here referred as the Palu–Lake Hazar segment (PLHS; Fig. 1b). To the northeast of the PLHS is the Karlıova–Bingöl segment (KBS; Fig. 1b), part of which ruptured in the 1971 Bingöl earthquake (Arpat and Saroglu, 1972; Seymen and Aydın, 1972; Jackson and McKenzie, 1984). To the southwest of the PLHS is the Lake Hazar–Sincik segment (LHSS; Saroglu et al., 1992, Fig. 1b), separated from the PLHS by the Lake Hazar.

Eastern Anatolia is one of the best examples of an active continental collision zone in the world. It comprises one of the high plateaus of the Alpine–Himalaya mountain belt which is covered by young volcanic units related to collision (Pearce et al., 1990; Yilmaz et al., 1998; Keskin, 2003, 2005; Keskin et al., 2006) with an age ranging from 11 Ma to recent and a thickness of up to 1 km in places. Recent volcanic activity in Turkey is closely related to the tectonic evolution of the Alpine–Mediterranean belt. The location, timing and geochemical characteristics of volcanism result from the complex interaction of the colliding Eurasian and Afro-Arabian plates. Neogene–Quaternary

volcanism in Turkey is closely associated with neotectonic evolution. Quaternary volcanism is confined to the Kula area in western Anatolia, whereas the recent volcanoes are more abundant in central and especially in eastern Anatolia where the latest eruptions took place at Nemrut volcano in 1692 (Tchalenko, 1977). The contemporary existence of active tectonics and very recent volcanic activity has a strong impact on the geochemistry of the circulating fluids. Fig. 2 shows geological sections typical for the investigated segments of the EAFZ. Moving from NE (Tekman–Erzurum) towards SW (across Hınıs and Varto–Muş, Bingöl, Karakocan–Elazığ and Ispendere–Malatya) the superficial levels contain travertine (indication of CO<sub>2</sub> degassing from the waters) at all the sites. Volcanites, made by basaltic products, are of Miocene age at the sites of Erzurum, Muş, Bingöl, and Elazığ (Fig. 2a, b, c, d) and of Cretaceous age at the Malatya area (Fig. 2e).

The release of volcanic fluids is a common feature along the main active faults in Turkey, however the local geological setting is responsible for the uprising of deep fluids through the tectonic discontinuities and the occurrence of shallow processes affecting the original characteristics of the circulating fluids. Moreover, the presence of carbonatic rocks, travertine deposits, metamorphic rocks and old volcanites (Fig. 2) accounts for a different nature of the circulating fluids and different fluid–rock interactions.

### 3. Methods

#### 3.1. Field investigations

Table 1 lists the type and location (given in UTM-WGS84 coordinates) of 16 sites along three different segments of the EAFZ where a total of 21 samples (11 bubbling and 10 dissolved gas samples), were collected (Fig. 1b). Some of the sampled springs were totally unknown and discovered by an accurate field work and located on the map by GPS. On the field, the samples were collected following already adopted methodologies for bubbling and dissolved gases (Italiano et al., 2009).

The dissolved gases were extracted from water samples collected in 240 ml glass bottles sealed in the field by silicon/rubber septa using special pliers. All of the samples were collected taking care to avoid even tiny bubbles to prevent atmospheric contamination (details in Italiano et al., 2009).

The bubbling gases were collected using a stainless-steel inverse funnel connected to a three way valve. The valve was connected to a syringe and to a two-way pyrex bottle with vacuum stop-cocks at both ends. The syringe sucked the gas collected by the funnel and through the valve, the gas was pushed inside the sampling bottle. The bottle

**Table 1**  
Field information of the sampled gases. See Fig. 1 for sample locations over the EAFZ. D stands for dissolved gases, B for bubbling. T °C is the highest outlet temperature of the spring. n.m. = not measured. Coordinates in UMTS WGS84. See Fig. 1b for segment names and for segment and sample location.

Sample ID	Site name	Segment N°	Type	T °C	Latitude	Longitude	Altitude
I-1	Ispendere–Malatya	3	D	23.8	37S462943	4245064	822
I-2	Ispendere–Malatya	3	B	21.1	37S462940	4245069	823
B-1	Bagın (Mazgirt)–Tunceli	2	B	36.6	37S577706	4317291	953
G-1	Golan (Karakoçan)–Elazığ	2	B	43.5	37S576940	4316638	941
SL-1	Sülüklü (Karakoçan) spring	1	D	17.0	37S579505	4318723	980
SL-2	Sülüklü (Karakoçan) mud–Tunceli	1	B	n.m.	37S579461	4318747	973
K-1	Kös–Bingöl	1	B/D	44.5	37S644701	4316960	1162
H-1	Hacılar (hill)(Karlıova)–Bingöl	1	B/D	67.3	37S655772	4328745	1580
H-2	Hacılar (Goynük river) (Karlıova)–Bingöl	1	D	46.0	37S656575	4328262	1368
Y-1	Yayladere–Bingöl	1	B	33.0	37S593156	4339762	1335
S-1	Sabırtasi (Kigi)–Bingöl	2	B/D	48.1	37S601948	4347546	1297
S-2	Sabırtasi (Kigi) near river Bingöl	2	D	41.2	37S601244	4347212	1170
C-1	Çatak–Karlıova–Bingöl	1	B/D	29.7	37S668292	4360782	1708
HM-1	Hamzan (Çatak)–Erzurum	1	D	54.8	37S684201	4369532	1945
HM-2	Hamzan(Çatak)–Erzurum	1	B	52.2	37S684166	4369490	1941
HM-3	Hamzan (Çatak)–Erzurum	1	D	41.1	37S684013	4369385	1938
GZ-1	Guzelkent–Varto–Muş	Varto Fault zone	B	27.5	37S697885	4346088	1523

was flushed with a gas ten times larger than its volume, and then the sample was collected following always the same procedure: the first valve is closed; the syringe applies a slight overpressure inside the bottle; and the second valve is finally closed.

### 3.2. Analytical methods

The chemical composition in terms of He, H<sub>2</sub>, O<sub>2</sub>, N<sub>2</sub>, CO, CH<sub>4</sub> and CO<sub>2</sub> contents was carried out using a Perkin Elmer Clarus 500 gas chromatograph equipped with a double detector (TCD-FID; detection limits 1 ppm/vol), with argon as carrier gas.

The bubbling gases were analyzed by direct injection in the gas-chromatograph, while the dissolved gas analyses were carried out on the gas phase extracted after the attainment of the equilibrium (at constant temperature) between the water sample and a known volume of host, high purity gas (argon), injected inside the sampling bottle (see Sugisaki and Taki, 1987 and Capasso and Inguaggiato, 1998 for details).

The isotopic compositions of helium and carbon were determined by mass spectrometry. Helium isotope analyses of both bubbling and dissolved gases (on gas fractions extracted following the same procedure as for the gas-chromatography and using nitrogen as host gas) were carried out after accurate sample purification following the already proposed procedures (e.g. Italiano et al., 2009). The isotopic analyses of the purified helium fractions were performed by a split flight tube static vacuum mass spectrometer (GVI5400TFT) that allows the simultaneous detection of <sup>3</sup>He and <sup>4</sup>He-ion beams, thereby keeping the <sup>3</sup>He/<sup>4</sup>He error of measurement to very low values. Typical uncertainties in the range of low-<sup>3</sup>He (radiogenic) samples are within ± 1%.

The water samples for dissolved gas analyses were also used for the determination of the carbon isotopic ratio of the total dissolved inorganic carbon (TDIC). The method for δ<sup>13</sup>C<sub>TDIC</sub> determination is based on the chemical and physical stripping of CO<sub>2</sub>. The stripped gas, as well as the bubbling CO<sub>2</sub>, are purified by means of standard procedures (Favara et al., 2002), then the carbon isotopic composition was measured using a Finnigan Delta Plus mass spectrometer and the results are expressed in ‰ vs. V-PDB standard. The standard deviation of <sup>13</sup>C/<sup>12</sup>C ratio is ± 0.2‰.

## 4. Results

Table 2 lists the analytical results of the gas-chromatographic analyses. The composition of the bubbling and dissolved gases are reported as vol% and cm<sup>3</sup> STP/L of water, respectively. The composition of the dissolved gas phase was calculated starting from the gas-chromatographic analyses and taking into account the solubility coefficients (Bunsen coefficient “β”, c<sub>gas</sub>/mL<sub>water</sub> STP) of each gas species, the volume of gas extracted (cm<sup>3</sup>) and the volume of the water sample, following Eq. (1):

$$G_C = \left\{ [G_{gc}] * V\gamma_e + \left( [G_{gc}] * \beta_G * VW \right) \right\} VW^{-1} * V\gamma_e * V\gamma_i^{-1} / 100 \quad (1)$$

where G<sub>C</sub> is the concentration of the selected gas specie, G<sub>gc</sub> is its concentration measured by the gas chromatograph (vol%), V<sub>γ<sub>e</sub></sub> and V<sub>γ<sub>i</sub></sub> represent the extracted and the introduced gas volumes respectively, while VW is the volume of the analyzed water sample (see also Italiano et al., 2009 for further details).

Assuming that the detected oxygen comes from the atmosphere and since any deep-originated gas is considered oxygen-free; we recalculated the gas analyses by removing the atmospheric contribution (analytical oxygen content versus its theoretical amount in ASW and in the air).

Moreover, starting from the total amount of dissolved gases (cm<sup>3</sup>/L at 20 °C) we calculated the relative abundances for every single gas species and normalized to 100% the analytical results, allowing a comparison of the analytical results of both dissolved and bubbling gases. The converted gas analyses (Cvt) are shown in columns 9–13 of Table 2.

Table 2 shows that 13 out of the 21 collected samples have a CO<sub>2</sub> concentration above 90 vol.% with a minimum content of 24.1%. N<sub>2</sub> varies over a small range in the dissolved gases, while it spans over a range of three orders of magnitude in the bubbling gases (0.03–73%). Helium, ranging from 10<sup>−6</sup> to 10<sup>−2</sup> vol.%, varies over a range of 2 and 3 orders of magnitude in dissolved and bubbling gases respectively. The reactive gases CO and CH<sub>4</sub> are always present with significantly lower concentrations from 10<sup>−6</sup> to 10<sup>−3</sup> vol.% the former and from 10<sup>−6</sup> to 10<sup>−1</sup> vol.% the latter (Table 2).

**Table 2**

Chemical composition of dissolved (D) and bubbling (B) gases from the various segments of the EAFZ. Data in columns from 3 to 8 show original gas concentrations expressed in ccSTP for dissolved gases and vol.% for bubbling. Columns from 9 to 13 show the results converted in vol.% after air removal recalculations based on oxygen content (see text for details). Values for ASW (Air Saturated Waters) are reported as reference (in italics).

1	2	3	4	5	6	7	8	9	10	11	12	13
Sample ID	Type	He	O <sub>2</sub>	N <sub>2</sub>	CO	CH <sub>4</sub>	CO <sub>2</sub>	He (Cvt)	N <sub>2</sub> (Cvt)	CO(Cvt)	CH <sub>4</sub> (Cvt)	CO <sub>2</sub> (Cvt)
I-1	D	6.7E−05	0.13	1.80	5.31E−04	7.95E−04	1210.8	5.5E−06	0.13	4.4E−05	6.6E−05	99.9
SL-1	D	bdl	0.11	2.21	2.37E−04		1857.2		0.12	1.3E−05		99.9
S-1	D	9.1E−05	0.11	5.66	1.54E−05	9.22E−04	194.1	4.5E−05	2.83	7.7E−06	4.6E−04	97.1
S-2	D	8.6E−05	1.56	7.97	4.27E−05	4.61E−04	333.5	2.2E−05	2.32	1.2E−05	1.3E−04	97.2
K-1	D	6.3E−05	0.28	2.23	3.83E−05	1.44E−03	464.9	1.3E−05	0.48	8.2E−06	3.1E−04	99.5
H-1	D	1.0E−04	0.10	2.82	1.47E−05	2.36E−04	181.6	5.4E−05	1.53	8.0E−06	1.3E−04	98.4
H-2	D	8.6E−05	6.77	22.01	1.59E−05	2.04E−04	219.2	1.2E−05	8.87	6.4E−06	8.2E−05	88.4
C-1	D	2.2E−04	0.30	6.52	0.00E+00	1.67E−03	66.4	3.0E−04	8.90		2.3E−03	90.7
HM-1	D	2.2E−04	1.13	4.29	1.32E−05	5.45E−05	267.1	8.0E−05	1.57	4.8E−06	2.0E−05	98.0
HM-3	D	1.1E−04	1.10	5.98	1.07E−05	2.18E−03	296.9	3.5E−05	1.97	3.5E−06	7.2E−04	97.7
ASW		4.1E−05	4.80	9.60	<i>n.d.</i>	<i>n.d.</i>	0.2	2.8E−04	65.60	<i>n.d.</i>	<i>n.d.</i>	1.6
I-2	B	4.0E−04	6.84	28.72	2.2E−03	1.4E−03	64.4	4.2E−04	20.38	2.3E−03	1.5E−03	68.1
B-1	B	1.1E−05	bdl	0.03	2.9E−04	1.3E−03	99.9	1.1E−05	0.03	2.8E−04	1.3E−03	99.8
SL-2	B	2.9E−04	4.48	18.22	8.2E−04	4.7E−03	77.3	3.1E−04	14.94	8.5E−04	4.9E−03	80.7
G-1	B	4.5E−05	3.15	12.24	7.1E−04	5.1E−05	84.6	4.7E−05	10.90	7.4E−04	5.3E−05	88.8
Y-1	B	1.1E−02	10.48	26.88	8.3E−03	3.7E−02	62.6	1.2E−02	15.58	9.6E−03	4.3E−02	73.1
S-1	B	1.4E−05	0.02	0.06	1.1E−04	4.3E−03	99.9	1.4E−05	0.06	1.1E−04	4.3E−03	99.8
K-1	B	4.1E−04	2.24	10.64	5.1E−04	1.7E−02	87.1	4.2E−04	9.70	5.2E−04	1.7E−02	89.0
H-1	B	1.2E−05	0.31	1.20	4.1E−04	2.7E−03	98.5	1.2E−05	1.18	4.1E−04	2.7E−03	98.7
C-1	B	5.0E−02	2.68	73.14	3.0E−05	8.3E−02	24.1	5.1E−02	64.38	3.1E−05	8.4E−02	24.3
HM-2	B	8.3E−03	0.04	16.67	1.0E−04	2.9E−01	83.0	8.1E−03	16.27	9.9E−05	2.8E−01	81.2
GZ-1	B	6.2E−05	bdl	0.15	3.0E−05	2.4E−04	99.8	6.2E−05	0.15	3.0E−05	2.4E−04	99.8



Table 3 lists the isotopic composition of helium and carbon as well as the  $^4\text{He}/^{20}\text{Ne}$  ratios. The  $^3\text{He}/^4\text{He}$  ratios (R) have been normalized to the atmosphere ( $^3\text{He}/^4\text{He} = 1.39 \times 10^{-6} = \text{Ra}$ ) and corrected for the effects of atmospheric contamination ( $\text{R}/\text{Ra}_c$ ) using  $(\text{R}/\text{Ra}_c) = \{(\text{R}/\text{Ra})X - 1\} / \{X - 1\}$  where X is the air and the ASW He/Ne ratio (Hilton et al., 1998) respectively for bubbling and dissolved gases. Carbon isotopic ratios of TDIC and  $\text{CO}_2$  express in  $\delta\text{‰}$  versus the PDB international standard. The last column of Table 3 shows the estimated equilibrium temperatures (in  $^\circ\text{C}$ ) for the bubbling gases (see Section 5.2 for details).

## 5. Discussion

### 5.1. Chemical composition

The variability of the gas composition has no relationships with the geographical location of the sampled fluids (see Fig. 1b). Contrastingly, we can recognize that the presence of  $\text{CO}_2$ -dominated gases is a common feature of all the investigated EAFZ segments and for the whole Karlova triple junction area. The presence of  $\text{N}_2$  and  $\text{O}_2$  in the sampled gases is clearly due to atmospheric contamination that occurred because of either the intense bubbling (trapped air bubbles) or mixing of shallow air-saturated ground waters (ASW) with waters of deeper provenance. Although variable extents of atmospheric contamination are detectable in bubbling and dissolved gases, He content is always in the concentrations well above the atmospheric, in agreement to the common feature that deep originated gases are  $\text{CO}_2$ -dominated and bring mantle and/or crustal-type helium.

Combining the information from both dissolved and bubbling gases, it is easy to find that although the  $\text{CO}_2$  content is often above 90%, some  $\text{CO}_2$  gas was already lost because of its fast gas dissolution in ground waters. Such an interaction between the upraising gases and the circulating waters (hereafter indicated as gas–water interactions, GWI) allowing undefined amounts of the deep originated gases to dissolve as a function of their solubility properties and the water/gas mass ratios. This occurrence, as discussed in the next sections, does not affect very much our results and interpretations.

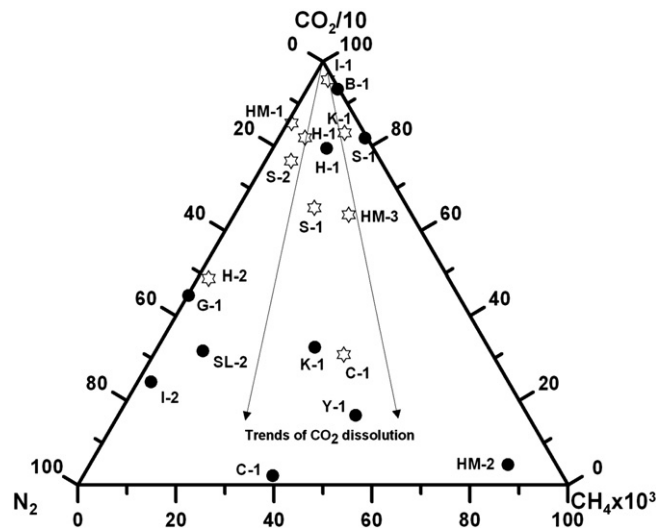


Fig. 3.  $\text{CH}_4$ – $\text{CO}_2$ – $\text{N}_2$  relationships for bubbling (filled black circles) and dissolved gases (empty stars). The arrows show GWI effects with various extents of  $\text{CO}_2$  dissolution. The occurrence of such a process explains the relative increased concentrations of nitrogen and  $\text{CH}_4$ .

### 5.2. GWI and geothermal systems

The GWI extent is testified by the composition of the gas assemblage. As a common feature, although  $\text{CO}_2$  always shows the highest content in bubbling and dissolved gases (Table 2), the less soluble species (He,  $\text{N}_2$ ,  $\text{CH}_4$ ) denote concentrations well above the equilibrium with the ASW. Moreover, He,  $\text{CH}_4$  and  $\text{N}_2$  concentrations in the bubbling gases, as reported for the recalculated values after air removing, show significant enrichments up to 64%  $\text{N}_2$  at C1,  $1.2 \times 10^{-2}\%$  He at Y1 and 0.28%  $\text{CH}_4$  at HM2.

The  $\text{CH}_4$ – $\text{N}_2$ – $\text{CO}_2$  triangular diagram of Fig. 3 displays the relative abundances for both dissolved and bubbling gases. The arrows indicate trends for  $\text{CO}_2$  loss due to GWI processes with the consequent

**Table 3**  
Isotopic composition of helium and carbon for dissolved (D) and bubbling gases (B).  $\text{R}/\text{Ra}_c$  denotes  $^3\text{He}/^4\text{He}$  ratios normalized to the atmospheric ratio ( $\text{Ra} = 1.39 \times 10^{-6}$ ) and corrected for the atmospheric contamination (see text for details).  $\Delta \text{He}/\text{Ne}$  ( $\text{He}/\text{Ne}$  sample/ $\text{He}/\text{Ne}$  air) shows how many times the measured He/Ne is larger than the atmospheric ratio. The  $\text{CO}_2/^3\text{He}$  data are  $\times 10^9$  calculated from Table 1/columns 9–13.  $T$   $^\circ\text{C}$  is the estimated geotemperature for bubbling gases. Data for ASW and AIR are reported as references ( $^4\text{He}/^{20}\text{Ne}$  ratio of air-saturated water is taken as 0.285). Carbon isotopic ratios expressed as  $\delta\text{‰}$  PDB. n.d. = not determined. Values for ASW and AIR are reported as reference (in italics).

Type	Sample ID	Site name	R/Ra	He/Ne <sub>m</sub>	$\Delta \text{He}/\text{Ne}$	R/Ra <sub>c</sub>	$\delta^{13}\text{C}$	$\text{CO}_2/^3\text{He}$	T $^\circ\text{C}$
D	I-1	İspendere	0.77	0.49	1.7	0.44	0.35	17121	n.d.
D	S-1	Sabirtasi Kigi	0.87	0.44	1.5	0.63	2.68	n.d.	n.d.
D	S-2	Sabirtasi Kigi near river	1.12	0.32	1.1	1.95	0.68	3723	n.d.
D	K-1	Kös	1.04	0.39	1.4	1.15	2.17	5294	n.d.
D	H-1	Hacılar (hill)	1.07	0.34	1.2	1.42	3.01	1221	n.d.
D	H-2	Hacılar (Goynük river)	1.02	0.45	1.6	1.06	3.41	5153	n.d.
D	C-1	Çatak Karlıova	1.17	1.05	3.7	1.23	0.59	183	n.d.
D	HM-1	Hamzan (Çimenözü) Çatak	1.02	1.49	5.2	1.03	3.4	857	n.d.
D	HM-3	Hamzan (Çimenözü) Çatak	1.02	0.52	1.8	1.03	n.d.	2005	n.d.
B	I-2	İspendere borehole	1.05	0.36	1.1	1.41	−4.41	110	328
B	B-1	Bagın Mazgirt	1.71	0.69	2.2	2.32	−4.20	3968	263
B	SL-2	Sülüklü Mazgirt mud	2.86	0.70	2.2	4.41	n.d.	65	300
B	G-1	Golan	0.47	1.46	4.6	0.32	−0.94	2906	325
B	Y-1	Yayladere	1.87	7.46	23.5	1.91	−5.67	2.3	344
B	S-1	Sabirtasi Kigi	2.01	1.45	4.5	2.30	−2.40	2567	222
B	K-1	Kös	2.38	3.70	11.6	2.51	−1.23	65	265
B	H-1	Hacılar (hill)	2.26	1.68	5.3	2.55	−1.20	2515	270
B	C-1	Çatak Karlıova	1.54	25.50	80.2	1.54	n.d.	0.2	193
B	HM-2	Hamzan (Çimenözü) Çatak	1.07	29.11	91.5	1.07	−0.20	6.7	192
B	GZ-1	Guzelkent Varto	4.00	17.93	56.4	4.06	−1.79	289	204
	ASW		1	0.285			n.d.	n.d.	
	AIR		1	0.318			−7	n.d.	

enrichment of CH<sub>4</sub> and N<sub>2</sub>. As example, sample C1 underwent enhanced GWI as shown by the low CO<sub>2</sub> concentration of the bubbling gases (24%) and the large content of the low soluble species. The distribution of the low-solubility species He, CH<sub>4</sub> and N<sub>2</sub> is displayed in Fig. 4. Samples C1 and Y1 belong to a group of bubbling gases (including S1, B1 and HM2, Fig. 4) falling on a CH<sub>4</sub>-enrichment trend with an almost constant He/N<sub>2</sub> ratio. The reported analyses (Table 2) clearly show the absence of significant air contamination at S1, HM2 and B1 sites. Contrastingly, large amounts of both O<sub>2</sub> and N<sub>2</sub> are detected at Y1 and C1 (10.48 and 2.68% of O<sub>2</sub>, respectively) besides relatively large amounts of both He (1.1 and 5 × 10<sup>-2</sup>%) and CH<sub>4</sub> (3.7 and 8.3 × 10<sup>-2</sup>%). Sample K<sub>1</sub> shows larger CH<sub>4</sub>, N<sub>2</sub> and He enrichment in the bubbling gases than in the dissolved gas phase. We argue that the enrichment of low soluble species may have occurred well before the air contamination, thus in deep-located water bodies where massive amounts of CO<sub>2</sub> had been able to dissolve and, consequently, significantly enhanced the He, N<sub>2</sub> and CH<sub>4</sub> contents. Contrastingly, air contamination (see C1 and Y1 analyses; Table 2) seems to have occurred at very shallow levels, close to the sampling point due to the active gas bubbling.

Although the deep originated gases interact and probably equilibrate in deep aquifers before upraising to the surface, the evidence of the low CO<sub>2</sub> concentration (66 cm<sup>3</sup> STP/L, far away from the CO<sub>2</sub> saturation in water of 762 cm<sup>3</sup> STP/L; Weiss, 1971) besides the enhanced helium content (2.2 × 10<sup>-4</sup> cm<sup>3</sup> STP/L) in the dissolved gases at C1 site, leads us to expect the occurrence of repeated subsurface GWI processes responsible for CO<sub>2</sub> removing from the gas phase.

Despite the occurrence of GWI processes, the concentrations of the reactive species CO and CH<sub>4</sub> are generally low in both dissolved and bubbling gases (Table 2), showing insignificant contribution of hydrocarbon sources along the explored EAFZ segments.

It is worthy of notice that the CH<sub>4</sub> content (that at Y1, C1 and HM2 exhibits the highest content among the collected samples) falls in the range of geothermal gas equilibriums (e.g. Fiebig et al., 2004 and references therein), providing clues, together with the emission temperatures of the collected gases (up to 67.3 °C), of a widespread presence of geothermal systems along the EAFZ.

In order to investigate such a possibility, we assume the existence of boiling aquifers where the deep boundary conditions (pressure, temperature, oxidation level) act as buffers for the chemical composition of the geothermal fluids. The reactive compounds detected in the sampled gases (CO, CH<sub>4</sub>, CO<sub>2</sub>), have been largely used for geothermometric and geobarometric considerations of hydrothermal fluids (e.g. Giggenbach, 1980; Italiano and Nuccio, 1991; Fiebig et al., 2004). The equilibrium

temperature of the gaseous species H<sub>2</sub>O, CO<sub>2</sub>, CH<sub>4</sub> and CO was estimated using the following reactions (Italiano and Nuccio, 1991):



and



For which the equilibrium constants, K, are (in logarithmic form):

$$\text{Log } K_1 = 2\text{Log}[(\chi\text{CO}_2)(\gamma\text{CO}_2)\text{Pt}(\chi\text{CO})^{-1}(\gamma\text{CO})^{-1}\text{Pt}] - \text{Log } f_{\text{O}_2} \quad (4)$$

$$\text{Log } K_2 = 1/2[(\chi\text{CO}_2)(\gamma\text{CO}_2)\text{Pt}(\chi\text{CH}_4)^{-1}(\gamma\text{CH}_4)^{-1}\text{Pt}] - \text{Log } f_{\text{O}_2} + \text{Log } f_{\text{H}_2\text{O}} \quad (5)$$

where  $\chi$  is the molar fraction,  $\gamma$  is the activity coefficient, Pt is the total pressure, and  $f$  is the fugacity.

Using numerical equilibrium constants for K<sub>1</sub> and K<sub>2</sub>, the  $f_{\text{O}_2}$  dependence for Eqs. (4) and (5) can be expressed as:

$$\text{Log } f_{\text{O}_2} = 2\text{Log}[\text{CO}_2]/[\text{CO}] - 29600/T + 9.6 \quad (6)$$

$$\text{Log } f_{\text{O}_2} = 1/2\text{Log}[\text{CO}_2]/[\text{CH}_4] - 23248/T + 6.51. \quad (7)$$

Finally, combining functions (6) and (7), the temperature dependence can be expressed in the general form:

$$T = B[1/2\text{log}(\chi\text{CO}_2)(\chi\text{CH}_4)^{-1} - 2\text{log}(\chi\text{CO}_2)(\chi\text{CO})^{-1} - A]^{-1} \quad (8)$$

where A and B are constants derived from K<sub>1</sub> and K<sub>2</sub>. The thermodynamic equilibrium constants (listed in Giggenbach, 1987) and the assumptions/limitations adopted from Italiano and Nuccio (1991) and Giggenbach (1987), make the temperature estimations reasonably valid in the range between 100 and 400 °C. Considering the higher CO<sub>2</sub> solubility in water than those of CO and CH<sub>4</sub>, we could expect that both the CO<sub>2</sub>/CO and CO<sub>2</sub>/CH<sub>4</sub> ratios have been modified by gas–water interactions as suggested for some gas samples showing relatively low CO<sub>2</sub> contents (24 vol.% at C1). The adopted system, however, is more sensitive to the contents of CO and CH<sub>4</sub> than that of CO<sub>2</sub>, implying that although GWI induce modifications in the chemical composition, the estimated equilibrium temperatures do not change very much for, even large, variations of the CO<sub>2</sub> content. Moreover, the similar solubility coefficients of CO and CH<sub>4</sub> do not alter their abundance ratios, and their slow reaction kinetics allows them to keep the deep equilibrium conditions during the uprising. The Eq. (8) shows how the equilibrium constants are a function of temperature and oxygen fugacity, that changes due to the water molecule breaking (H<sub>2</sub>O = H<sub>2</sub> + 1/2O<sub>2</sub>) as a function of the temperature. The  $f_{\text{O}_2}$  is buffered by the mineral assemblage of the host rocks. The adopted buffers (QFM, HM and Ni–NiO; Eugster and Wones, 1962) are typical for silicatic (mainly volcanic) rocks where the contemporary presence of quartz, olivines, hematite, magnetite and nickel is able to keep the oxidation conditions within a narrow range as a function of the temperature (and pressure) of the geothermal boiling systems. Only the bubbling gases have been considered for geothermometric estimations and the plot of the results on a temperature– $f_{\text{O}_2}$  graph (Fig. 5a) shows that the samples fall between two theoretical  $f_{\text{O}_2}$  buffers proving that equilibrium is attained in every geothermal system. The estimated geotemperatures have been used to calculate the pressure of the geothermal system using the temperature–dependence function for 2 M NaCl solutions (Chiodini et al., 2001)

$$\text{log } f_{\text{H}_2\text{O}} = 5.479 - 2047/T. \quad (9)$$

Using the T–PH<sub>2</sub>O relationship for 2 M and NaCl saturated waters, the H<sub>2</sub>O pressure was estimated in the range from 13 to 195 bars. Fig. 5b shows the samples plotted besides the P–T curves together with the corresponding depth in terms of lithostatic pressure, assuming

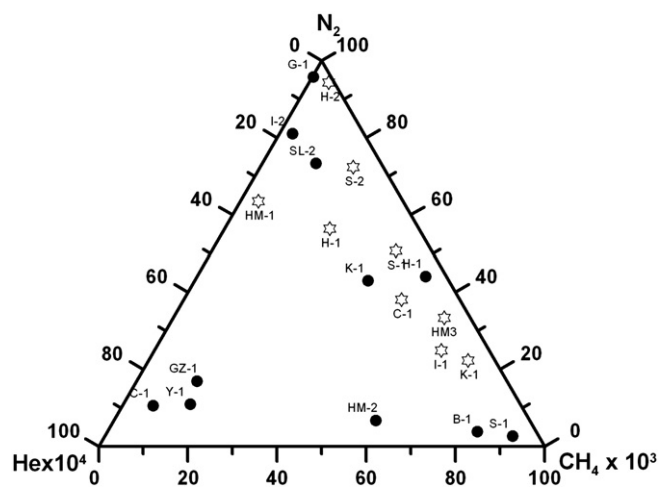
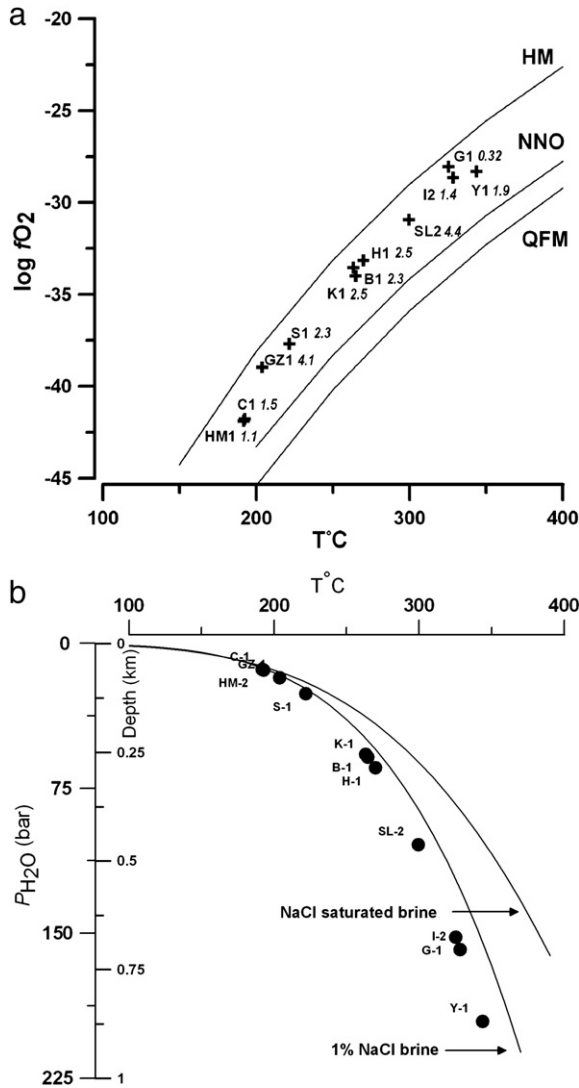


Fig. 4. Distribution of low-solubility gas species CH<sub>4</sub>, N<sub>2</sub> and He in bubbling and dissolved gases (symbols as in Fig. 2) along the EAFZ. The reported data are recalculated after air contamination removal (columns 9–13 in Table 2). CH<sub>4</sub> content accounts for equilibrations in high-temperature reservoirs while he and N<sub>2</sub> contents denote the extent of GWI processes.





**Fig. 5.** a) Temperature vs oxygen fugacity (expressed as  $\log fO_2$ ) graph. The equilibrium temperatures are estimated by Eq. (8); oxygen fugacity is calculated by introducing the estimated temperature value either in Eq. (6) or Eq. (7). The solid buffers quartz-fayalite-magnetite (QFM), nickel-nickel oxide (N-NO) and hematite-magnetite (HM) are plotted as reference (after Eugster and Wones, 1962). The sample distribution between the HM and NNO buffers denotes that they reflect equilibrium conditions in a relatively oxidizing system. The helium isotopic ratios are reported to show the absence of correlations with the estimated geotemperatures ( $R/R_a$  values in italics to the right of the sample labels). b) Estimated equilibrium pressure of the geothermal reservoirs. The pressure is shown on the vertical axis both as  $P_{H_2O}$  (bars) and depth (in km as lithostatic pressure). The boiling curves for saturated NaCl and 1%NaCl waters (brines) are shown.  $P_{H_2O}$  calculated after Italiano and Nuccio, 1991.

an average rock density of 2.4  $t/m^3$ . The helium isotopic ratios (Table 3), reported in Fig. 5a, show an evident lack of direct relationships between  $^3He/^4He$  ratios and estimated geotemperatures. We suggest that it can be the consequence of secondary processes (e.g. degassing, mixings of shallow and deep fluids) that affected the deep magmatic fluids at shallower levels. Relatively high  $^3He$  concentrations in low enthalpy waters have also been reported for the Northern Anatolia with no evidence of volcanic activity associated with the strike-slip motion along the seismically active segment of NAFZ (Gulec et al., 2002).

### 5.3. Helium isotopes

The measured helium isotopic ratios (reported as  $R/R_a$  where  $R$  = measured isotopic ratio and  $R_a$  = atmospheric  $^3He/^4He = 1.39 \times 10^{-6}$ ) have been corrected for the effects of atmospheric contamination

( $R/R_a$  values in Table 3) using the air-normalized  $He/Ne$  ratio and assuming that all the neon is of atmospheric origin. For dissolved gases the air-normalized  $He/Ne$  ratio is calculated taking also into account the ratio of their solubility coefficients (Bunsen coefficient “ $\beta$ ”, Weiss, 1971). The  $^3He/^4He$  and  $^4He/^{20}Ne$  ratios vary from 0.32 to 4.41  $R_a$  and from 0.32 to 29.1 (Table 2) respectively. The relationship between  $^3He/^4He$  and  $^4He/^{20}Ne$  ratios shows that all samples are a mixing of three end-members: primordial helium derived from the upper mantle, radiogenic helium produced from uranium and thorium in crustal rocks, and atmospheric helium dissolved in ground waters.

The  $He/Ne$  vs  $R/R_a$  graph of Fig. 6 shows mixing curves between atmospheric and mantle/crustal components assuming that an atmospheric component has  $^3He/^4He = 1.39 \times 10^{-6}$  and  $^4He/^{20}Ne = 0.318$ , and a crustal component has 0.02 $R_a$  and  $^4He/^{20}Ne = 1000$  (Sano and Marty, 1995). The presence of different mantle-type components are also considered: MORB-type mantle with 8 $R_a$  and  $^4He/^{20}Ne = 1000$ , Sub-Continental European Mantle (SECM, Dunai and Baur, 1995)  $R/R_a = 6.5$  and  $^4He/^{20}Ne = 1000$  and a possible mantle “contaminated” by crustal products due to subduction assumed to have  $^3He/^4He$  in the range of 2.5 $R_a$  and  $^4He/^{20}Ne = 500$ . The plot of our samples (only uncorrected  $^3He/^4He$  ratios have been used) shows the large atmospheric contamination of the dissolved gases (as expected) and the presence of a significant mantle component in the bubbling gases except for the site of Golan (G1 sample), clearly a mixture with radiogenic products.

The distribution of helium isotopes in Turkey has been investigated by several authors due to peculiar tectonic setting of this region where the tectonic movements of the Arabian, Eurasian and African plates take place (Fig. 1).  $^3He/^4He$  isotopic ratios have been measured along the NAFZ (Stone, 1986; Nagao et al., 1989; Kipfer et al., 1994; Ercan et al., 1995; Gulec, 1988; Gulec et al., 2002; de Leeuw et al., 2010), around the Marmara sea (Dogan et al., 2009), at the East Anatolia volcanic area (Stone, 1986; Nagao et al., 1989; Ercan et al., 1995; Pfister et al., 1997) in Western Anatolia (Mutlu et al., 2008) and along the EFZ (Nagao et al., 1989; Ercan et al., 1995). The data have coherently shown the presence of a magmatic helium component in regions of Neogene-Quaternary volcanics as well as in areas struck by the most

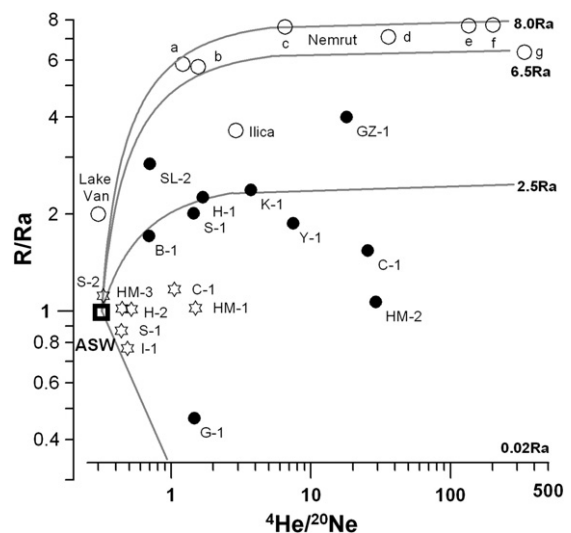


**Fig. 6.** Helium isotopic ratios (as  $R/R_a$  values) and  $He/Ne$  relationships. The theoretical lines represent binary mixing trends of atmospheric helium with mantle-originated and crustal helium. The assumed end member values for  $He$ -isotopic ratios mark the mixing curves: crust 0.02 $R_a$  and three different mantle-signatures: 8 $R_a$  (MORB); 6.5 $R_a$  (SECM) and 2.5 $R_a$  for a contaminated/degassed mantle (see text for details). Bubbling (black filled circles) and dissolved (stars) samples are plotted besides literature data for comparison (open circles). Data for Nemrut volcanic area are from Kipfer et al. (1994) (samples marked as a, b, d, e and Lake Van); Nagao et al. (1989) and Ercan et al. (1995) for sample c; Stone (1986) for Ilica; and Mutlu et al. (2012) samples f and g.

recent seismic events of NAFZ where, in contrast, no mantle products are recognized (Gulec et al., 2002). The highest ratios (4.41Ra<sub>c</sub> at Suluklu and 4.06Ra<sub>c</sub> at Guzelkent Varto), match the values measured at Ilica (Stone, 1986) and are lower than the highest values measured at the Nemrut volcanic area (up to 7.7Ra<sub>c</sub>; Kipfer et al., 1994; Mutlu et al., 2012).

The commonly accepted model that mantle-He correlates well with tectonic and magmatic activities (Polyak and Tolstikhin, 1985) and leads primordial <sup>3</sup>He inputs to occur in areas often associated with young volcanism (O'Nions and Oxburgh, 1988; Marty et al., 1992) seems to fail in some areas of the North and East Anatolian Fault Zones, where helium with magmatic signature does not correlate with evident magmatic activity. This evidence figures out that <sup>3</sup>He is degassed to the atmosphere from magmas intruded at shallow levels in the crust for example as already recognized in the Southern Apennines (Italiano et al., 2000). Alternatively, magmatic intrusions may have been shifted from their original location by the 10 mm/year strike-slip (left-lateral) motion of the EAFZ (Reilinger et al., 2006).

The active tectonic structures act as preferential escaping routes for any fluid, and the presence of a significant magmatic component in the fluids vented along the EAFZ, indicates that we are dealing with deep lithospheric discontinuities joined to cooling magma batches that are still able to release <sup>3</sup>He as well as thermal energy. Fig. 1b shows the distribution of magmatic products due to Miocene and Quaternary volcanism (after Cetin et al., 2003). Our sampling locations fall over areas involved in Neogene–Quaternary volcanism (but sampling site of Ispendere) although we didn't find a direct helium–heat correlation coupling the results of geothermometric estimations and helium isotopic ratios (Fig. 5a). Sample I1 (Ispendere, Table 3), collected far away the volcanic areas, has a helium isotopic ratio of 1.41Ra, while G1 (Golan) displays the lowest value (0.32Ra<sub>c</sub>) despite its location in a volcanic area. To give an explanation of those apparently inconsistent results, we observe that a considerable contribution of crustal <sup>4</sup>He comes from metamorphic rocks, old volcanites and carbonates. As synthesized in Fig. 2, the local geological sequence is responsible for the amount of radiogenic helium supplied to the deep mantle-originated fluids. Moreover, strong gas–water–rock interactions occur at crustal levels as demonstrated by the huge travertine deposits at Hacilar (2.55Ra<sub>c</sub> in bubbling gases) or the massive travertine covering at Bagin and Golan (2.32 and 0.32Ra in bubbling gases respectively) inducing further modifications to the pristine helium signature mainly due to degassing and atmospheric contamination. The distribution of helium isotopic ratios versus the He/Ne ratios is shown in Fig. 6 where binary mixing curves display the trends drawn by mixtures of the atmosphere with different mantle and crustal sources. The sample from Golan (G1) falls close to mixing curve with crustal helium, while the samples from Bagin, Hacilar, Kos, Sabirtasi and Yayladere follow a trend drawn by helium from a degassed mantle which isotopic ratio is assumed to be 2.5Ra (other curves have assumed as end members MORB-type helium and SECM-helium; Subcontinental European Contaminated Mantle; Dunai and Baur, 1995).

#### 5.4. Carbon isotopes

The various CO<sub>2</sub> sources, normally marked by different <sup>δ</sup><sup>13</sup>C ratios (<sup>δ</sup><sup>13</sup>C = 6.5‰ in MORB; 0‰ limestones, –20‰ marine sediments; –70 ÷ –30‰ organic sources; Faure, 1986; Javoy et al., 1986; Sano and Marty, 1995), may produce similar <sup>δ</sup><sup>13</sup>C values by admixtures of different sources. Moreover, because of its reactivity, CO<sub>2</sub> may suffer large <sup>δ</sup><sup>13</sup>C variability due to a wide spectrum of secondary processes (e.g. isotopic fractionation, isotopic equilibrium, chemical reactions, etc.) that modify both the original CO<sub>2</sub> content and its isotopic signature. The <sup>δ</sup><sup>13</sup>C data listed in Table 3, show that the isotopic composition of the vented and dissolved carbon from the EAFZ spans from –5.67‰ (Y1) to +3.4‰ (H2 and HM1) ruling out significant contributions from organic CO<sub>2</sub>. The relationship between the CO<sub>2</sub> content and its isotopic

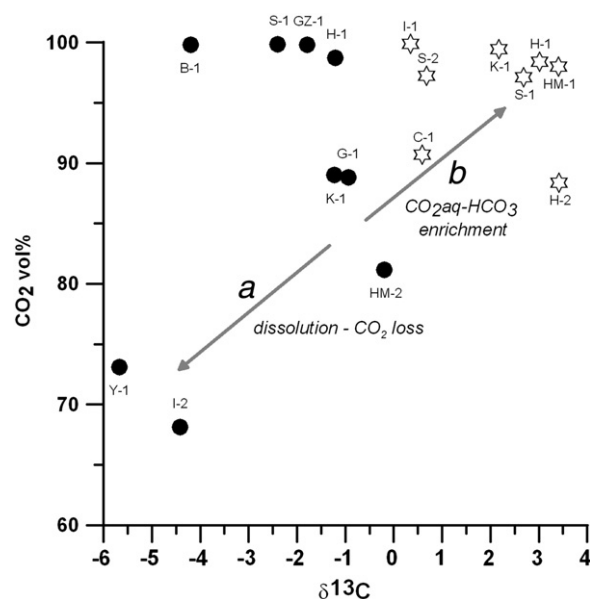


**Fig. 7.** CO<sub>2</sub> content vs <sup>δ</sup><sup>13</sup>C. The samples are distributed following a trend of direct CO<sub>2</sub> content–isotopic ratio correlation. The lines *a* and *b* denote the fractionation trend: *a*) quantitative loss of gaseous CO<sub>2</sub> due to dissolution, and *b*) enrichment in the liquid phase of aqueous CO<sub>2</sub>, bicarbonate ions and <sup>13</sup>C. See text for further details.

composition is plotted in Fig. 7 roughly showing that the higher is the CO<sub>2</sub> content the higher is its isotopic ratio. The group of samples B1, S1, H1, and GZ1 (Fig. 7) for which no CO<sub>2</sub>–<sup>δ</sup><sup>13</sup>C relationship exists, can be representative of the isotopic equilibrium at the level of the geothermal reservoir where GWI occurred. Moreover, as those samples show also the lowest oxygen contents (Table 2, column 4) it indicates negligible GWI with ASW at shallower levels. Positive <sup>δ</sup><sup>13</sup>C values (from +0.35‰ at Ispendere to +3.41‰ at Hacilar) are a common feature of the dissolved carbon (TDIC) as a consequence of carbon fractionation due to dissolution processes and <sup>13</sup>C enrichment in the liquid phase.

The negative values of the bubbling gases are in agreement with the possibility that the EAFZ may degas CO<sub>2</sub> from mantle-derived products (cooling magma batches, mantle degassing), although the presence of CO<sub>2</sub> produced at crustal levels by secondary reactions including hydrolysis (Kissin and Pakhomov, 1967), and metamorphic decarbonation (Gianelli, 1985) seems to play a significant role as shown by the widespread presence of travertine deposits.

To better constrain the origin of the released CO<sub>2</sub> as well as possible secondary processes, we coupled the information coming from CO<sub>2</sub> with those from helium which, due to its chemical inertness, is only sensitive to mass fractionation and mixing processes.

The CO<sub>2</sub>/<sup>3</sup>He ratios span five orders of magnitude interval (2 × 10<sup>8</sup>–1.7 × 10<sup>13</sup>, Table 3 including bubbling and dissolved gases) with values always lower than the range considered as typical for crustal-type volatiles (1 × 10<sup>14</sup>; O'Nions and Oxburgh, 1988). The CO<sub>2</sub>/<sup>3</sup>He ratios don't show correlations with the helium isotopic ratios, revealing that for both dissolved and bubbling gases, local processes (e.g. GWI, degassing, calcite precipitation) have a significant impact on the elemental carbon/helium ratio.

Fig. 8 shows the He concentration versus CO<sub>2</sub>/<sup>3</sup>He ratio where samples coming from different segments of the EAFZ exhibit a negative correlation. The trend denotes significant changes of 5 orders of magnitude for both the helium content and CO<sub>2</sub>/<sup>3</sup>He ratio. The GWI processes are partially responsible for the observed pattern, however interactions of the deep gases with the circulating waters result in a CO<sub>2</sub> loss and consequent helium enrichment as in the case of the lowest CO<sub>2</sub>/<sup>3</sup>He ratios at Catak and Yayladere. Contrastingly, high CO<sub>2</sub>/<sup>3</sup>He ratios (e.g. Golan, Bagin, and Hacilar) in the order of 10<sup>13</sup> require an extra CO<sub>2</sub> production. CO<sub>2</sub> might be locally produced at a reservoir level by secondary reactions (carbonatic rock dissolution). Alternatively, due to the thermal

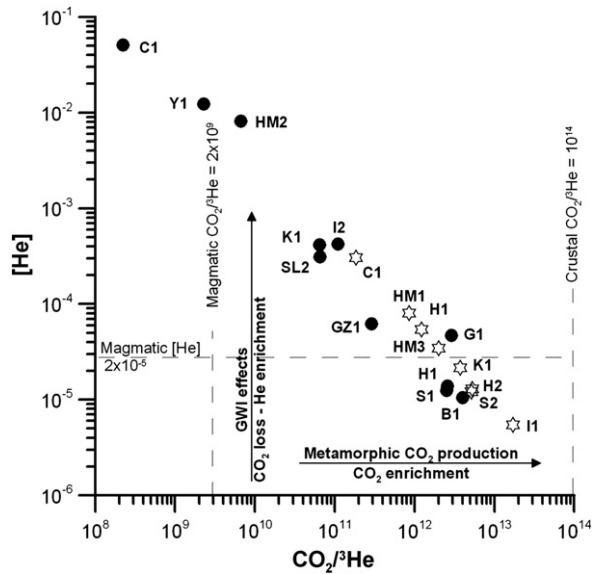


**Fig. 8.**  $\text{CO}_2/{}^3\text{He}$  ratio versus He concentration. The arrows display the trends of increasing ratio due to  $\text{CO}_2$  addition and increasing He content due to  $\text{CO}_2$  loss. The dashed lines mark the reported end members for magmatic  $\text{CO}_2/{}^3\text{He}$  ratio ( $2 \times 10^9$ , Marty and Jambon, 1987; Sano and Marty, 1995) and crustal ratio ( $10^{14}$ , O’Nions and Oxburgh, 1988) and the average concentration of magmatic He ( $2 \times 10^{-5}$  vol.%) in a MORB-type,  $\text{CO}_2$ -dominated gas (Paonita and Martelli, 2007).

energy released by magmatic rocks intruded in the sedimentary sequence, a metamorphic origin for the  $\text{CO}_2$  has to be considered.

Degassing of geothermal waters is able to fractionate the elemental  $\text{CO}_2$ -He ratio, thus justifying the low helium content for the G1, H1 and B1 sites.

### 5.5. Fluid/fault relationship model

The geochemical investigations have demonstrated to be a powerful tool to get insight on fluids’ origin and circulation in active tectonic environments. The observed features are consistent with a production/circulation model based on a mantle origin of the circulating fluids and shallower interactions affecting their original geochemical features.  $\text{CO}_2$ -dominated mantle volatiles move towards the surface through active faults bringing also helium with a magmatic signature. Mixings at various levels of the ascending mantle volatiles with crustal and atmospheric fluids and interactions with ground waters, modify the original gas assemblage in terms of both chemical and isotopic compositions (mainly referred to He and C). The results gained for the EAFZ, show that binary mixing between crustal and mantle-derived volatiles can explain the  ${}^3\text{He}/{}^4\text{He}$  ratios (corrected for the atmospheric contamination). Mass fractionation effects due to preferential He degassing from the geothermal waters and from magmatic bodies are responsible for the large variability of  $\text{CO}_2/{}^3\text{He}$  values along the EAFZ.  $\text{CO}_2$  production due to secondary dissolution reactions and metamorphic decarbonation, followed by calcite precipitation and GWI processes that lead to  $\text{CO}_2$  loss, are responsible for the final chemical composition of the volatiles released along the Fault.

Table 4 lists the magnitude and focal depths of the main seismic events that hit the area between 1950 and 2011. 11 out of the 25 strong earthquakes had focal depths  $\geq 25$  km (up to 50 km; Kandilli Observatory and Earthquake Research Institute web site). Since the crustal thickness of the area crossed by the EAFZ is estimated to be between 25 and 45 km (Arslan et al., 2010) it results that those hypocenters were located at the lower crust–upper mantle transition, clearly showing the lithospheric character of the various segments of the EAFZ. Such a tectonic setting supports the proposed provenance for the fluids which either are from the upper mantle or released from mantle-derived products (i.e. magmas).

**Table 4**

Strong earthquakes occurred over the EAFZ from 1950 to present. The magnitude and hypocentral depths are shown (Kandilli Observatory and Earthquake Research Institute web site).

Epicentral area	Date	M	Depth
Kığı–Bingöl	February 4, 1950	4.6	30
Pasinler–Erzurum	January 1, 1952	5.6	40
Hıms	October 10, 1959	5.0	50
Karlıova–Bingöl	August 31, 1965	5.6	33
Varto–Muş	March 7, 1966	5.6	26
Varto–Muş	August 19, 1966	6.9	26
Pülümür–Tunceli	July 26, 1967	6.2	30
Bingöl–Elazığ	September 24, 1968	5.1	8
Bingöl	May 22, 1971	6.7	3
Palu–Elazığ	March 26, 1977	5.2	25
Muş–Bulanık	March 27, 1982	5.2	38
Sürgü–Malatya	May 5, 1986	6.8	10
Sürgü–Malatya	June 6, 1986	5.6	11
Erzincan–Tunceli	March 13, 1992	6.8	27
Pülümür–Tunceli	January 27, 2003	6.2	10
Karakoçan–Elazığ	May 1, 2003	6.4	6–10
Sivrice–Elazığ	August 11, 2004	5.9	5
Karlıova–Bingöl	March 12, 2005	5.7	5
Karlıova–Bingöl	March 14, 2005	5.9	5
Karlıova–Bingöl	June 6, 2005	5.9	34.9
Sivrice–Elazığ	February 9, 2007	5.3	5
Sivrice–Elazığ	February 21, 2007	5.5	5
Karakoçan–Elazığ	March 8, 2010	6	5
Palu–Elazığ	March 24, 2010	5.1	4.5
İçme–Elazığ	June 23, 2011	5.4	6.1

Although the average mantle fluid flux from the continental crust is low (e.g.  ${}^3\text{He}$  flux in the order  $10^3$  atoms  $\text{cm}^{-1} \text{s}^{-1}$ ; O’Nions and Oxburgh, 1983), it may increase by 2–3 orders of magnitude because of magma intrusions (e.g. Martel et al., 1989) up to fluxes in the order of  $10^{10}$  atoms  $\text{cm}^{-1} \text{s}^{-1}$  along fault zones in Japan (Wakita et al., 1978) and  $10^{12}$  atoms  $\text{cm}^{-1} \text{s}^{-1}$  in Italy (Italiano et al., 2000) due to intracrustal magmatic bodies. The mantle fluids are driven to the surface by the enhanced vertical permeability of the faults. Permeability is usually the primary control on fluid flow and it varies by many orders of magnitude in common geologic media. As lithospheric pressure progressively closes fractures and voids, permeability decreases up to 6 orders of magnitude from the surface to a depth of 30 km (Criss and Taylor, 1986; Manning and Ingebritsen, 1999). The presence of deep lithospheric faults, however, may increase the rock permeability by 3–4 orders of magnitude (U.S. National Committee for Rock Mechanics, 1996), thus allowing a preferential and enhanced uprising path for the mantle fluids. The tectonic setting of the EAFZ, as shown by hypocenters’ location, allows draining of mantle helium that, because of the low (diffusive regime) flux, can easily modify its isotopic ratio with the addition of radiogenic  ${}^4\text{He}$  produced by different lithologies in the upper crust. Locally intruded magma bodies, probably from the widespread Neogene–Quaternary volcanic activity of East Anatolia, seem to be cooling down and, although too cold to make eruptions, they are still able to release thermal fluids with mantle signature. The long-term degassing induced significant mass fractionation that decreased the original MORB-type helium isotopic ratio (7.69Ra as observed at Nemrut volcano; Nagao et al., 1989; Ercan et al., 1995) to the measured low values. The interaction of the uprising magmatic fluids with shallow groundwaters generated high-T geothermal systems where deep fluids equilibrate and undergo GWI at deeper level if compared with further GWI occurring at shallower levels where atmospheric components contaminate the uprising fluids and add the air-derived components (mainly oxygen and neon) as detected by the analytical procedures. The escaping geothermal fluids rapidly move towards the surface following high permeability paths as shown by the chemical equilibrium of the bubbling gas assemblage.



## 6. Conclusions

The investigations carried out at three segments of the EAFZ, from Malatya to Karlıova, allowed us to gain an insight into the origin of the thermal fluids vented along the fault as well as into the fluid/fault relationships. Bubbling and dissolved gas samples have been collected from thermal waters with temperatures up to 67 °C and whatever is their final composition, the geochemical features of the collected gases show how they come from geothermal reservoirs heated up by deep mantle-derived fluids.

Deep originated fluids are released by diffusion from the upper mantle and by effusion from magmatic bodies intruded in deep crustal levels; the produced mantle fluids are drained by various segments of the EAFZ towards the surface; during their uprising they undergo interactions with cold and geothermal waters and with the hosting rocks as a function of the local geological setting. The estimated equilibrium temperatures ( $190 < T < 360$  °C) highlight the existence of several geothermal systems in all probability boiling under a hydrostatic pressure estimated, at most, close to 200 bars. It supports the assumption that the geothermal systems where GWI and other processes (e.g. degassing, dissolution) modify the deep gas assemblages and their geochemical features, are located at shallow levels in the upper crust.

The collected results show that deep originated (magmatic) fluids are driven to the surface by lithospheric discontinuities. The pristine gas phase, however, seems largely fractionated by several processes even though a basic role is attributable to the age of magmatism and the intensity of magmatic degassing. Both of the processes are able to fractionate helium by removing the lighter isotope thus changing the mixing proportion with crustal helium.

This study provides the first fluid/fault relationships modeling for an area where the crustal deformation is measured to be fast (20 mm/year; Sengör et al., 2008) thus able to accumulate stress and produce earthquakes in short times.

## Acknowledgments

This work was financially supported by FUBAP MF.11.12 Project (Firat University, Turkey) and INGV. The authors are grateful for the useful revision of two anonymous referees who greatly improved the paper. The authors are indebted to Mauro Martelli, Francesco Salerno, Andrea Rizzo, Fausto Grassa, Mariano Tantillo, Aldo Sollami, Igor Oliveri and Antonio Paonita (all from INGV-Palermo) for their help in the laboratory work and the stimulating discussions.

## References

- Aksu, A.E., Calon, T.J., Piper, D.J.W., Turgut, S., Izdar, E., 1992. Architecture of late orogenic Quaternary basins in northeastern Mediterranean Sea. *Tectonophysics* 210, 191–213.
- Ambraseys, N.N., 1989. Temporary seismic quiescence: SE Turkey. *Geophysical Journal* 96, 311–331.
- Ambraseys, N.N., Jackson, J.A., 1998. Faulting associated with historical and recent earthquakes in the Eastern Mediterranean region. *Geophysical Journal International* 133, 390–406.
- Arpat, E., Saroglu, F., 1972. Dogu Anadolu fayi ile ilgili bazı gozlem ve dusunceler (Some observations and thoughts on the East Anatolian fault). *Bulletin of the Mineral Research and Exploratory Institute of Turkey* 73, 44–50.
- Arslan, S., Akin, U., Alaca, A., 2010. Investigation of crustal structure of Turkey by means of gravity data. *Mineral Research Exploration Bulletin* 140, 55–71.
- Ates, R., Bayulke, N., 1977. 26 Mart 1977 Palu (Elazig) depremi [The March 26, 1977 Palu (Elazig) earthquake]. *Imar ve Iskan Bakanligi, Deprem Arastirma Enstitusu* (unpublished report).
- Barka, A.A., Kadinsky-Cade, K., 1988. Strike-slip fault geometry in Turkey and its influence on earthquake activity. *Tectonics* 7 (3), 663–684.
- Capasso, G., Inguaggiato, S., 1998. A simple method for the determination of dissolved gases in natural waters. An application to thermal waters from Vulcano island. *Applied Geochemistry* 13, 631–642 [http://dx.doi.org/10.1016/S0883-2927\(97\)00109-1](http://dx.doi.org/10.1016/S0883-2927(97)00109-1).
- Cetin, H., Guneyli, H., Mayer, L., 2003. Paleoseismology of the Palu–Hazar Lake Segment of the East Anatolian Fault Zone, Turkey. *Tectonophysics* 374, 163–197.
- Cetindag, B., Afsin, M., Canik, B., 1993. Ispendere (Malatya) Sıcak ve Mineralli İçmece kaynağının Hidrojeoloji İncelemesi. A. Suat Erk Jeoloji Sempozyumu Bildirileri, pp. 403–410 (in Turkish).
- Cetindag, B., Oztekin Okan, O., Kalender, L., Inceoz, M., Yıldırım, V., 2009. Hydrogeology and geochemistry of thermal and mineral waters in northwest of Karakoçan (Elazığ). Formation and Determination of Protection Areas of the Travertine Occurrences Related with These Waters: TUBİTAK 106Y150 Project, Final Report. 105 pp.
- Chiodini, G., Marini, L., Russo, M., 2001. Geochemical evidence for the existence of high-temperature hydrothermal brines at Vesuvio volcano, Italy. *Geochimica et Cosmochimica Acta* 65, 2129–2147.
- Criss, E.R., Taylor, H.P., 1986. Meteoric-hydrothermal system. In: Valley, J.W., Taylor Jr., H.P., O'Neil, J.R. (Eds.), *Stable Isotopes in High Temperature Geological Process: Rev. Mineral.*, 16, pp. 373–424.
- de Leeuw, G.A.M., Hilton, D.R., Gulec, N., Mutlu, H., 2010. Regional and temporal variations  $CO_2/{}^3He$ ,  ${}^3He/{}^4He$  and  $\delta^{13}C$  along the North Anatolian Fault Zone, Turkey. *Applied Geochemistry* 25, 524–539.
- Dogan, T., Sumino, H., Nagao, K., Notsu, K., Tuncer, M.K., Celik, C., 2009. Adjacent releases of mantle helium and soil  $CO_2$  from active faults: observations from the Marmara region of the North Anatolian Fault zone, Turkey. *Geochemistry, Geophysics, Geosystems* 10, Q11009 <http://dx.doi.org/10.1029/2009GC002745>.
- Dunai, T.J., Baur, H., 1995. Helium, neon and argon systematics of the European subcontinental mantle: implications for its geochemical evolution. *Geochimica et Cosmochimica Acta* 59, 2767–2783 [http://dx.doi.org/10.1016/0016-7037\(95\)00172-V](http://dx.doi.org/10.1016/0016-7037(95)00172-V).
- Ercan, T., Matsuda, J.I., Nagao, K., Kita, I., 1995. Noble gas isotopic compositions in gas and water samples from Anatolia. In: Erler, A., Ercan, T., Bingöl, E., Orcen, S. (Eds.), *Geology of the Black Sea Region: Proc. Int. Symp. on the Geology of the Black Sea Region*, Ankara, Turkey. General Directorate of Mineral Research and Exploration and the Chambers of Geological Engineers of Turkey, Ankara, pp. 197–206.
- Erisen, B., Akkuş, I., Uygur, N., Koçak, A., 1996. Türkiye Jeotermal Envanteri. Maden Tetkik ve Arama Genel Müdürlüğü Yayını, Ankara. 480 pp. (in Turkish).
- Eugster, H.P., Wones, D.R., 1962. Stability relation of the ferruginous biotite, annite. *Journal of Petroleum Science* 3, 82.
- Faure, G., 1986. *Principles of Isotope Geology*, 2nd Edition. Wiley, New York. 589 pp.
- Favara, R., Grassa, F., Inguaggiato, S., Pecoraino, G., Capasso, G., 2002. A simple method to determine the  $\delta^{13}C$  content of total dissolved inorganic carbon. *Geofisica Internazionale* 41 (3), 313–320.
- Fiebig, J., Chiodini, G., Caliro, S., Rizzo, A., Spangenberg, J., Hunziker, J.C., 2004. Chemical and isotopic equilibrium between  $CO_2$  and  $CH_4$  in fumarolic gas discharges: generation of  $CH_4$  in arc magmatic-hydrothermal systems. *Geochemistry Cosmic Acta* 68 (10), 2321–2334.
- Gianelli, G., 1985. On the origin of geothermal  $CO_2$  by metamorphic processes. *Bollettino della Società Geologica Italiana* 104, 575–584.
- Giggenbach, W.F., 1980. Geothermal gas equilibria. *Geochimica et Cosmochimica Acta* 44, 2021–2032.
- Giggenbach, W.E., 1987. Redox processes governing the chemistry of fumarolic gas discharges from White Island, New Zealand. *Applied Geochemistry* 2, 143–161.
- Gulec, N., 1988. He-3 distribution in western Turkey. *Bulletin. Mineral Research and Exploration Institute (Turkey)* 108, 35–42.
- Gulec, N., Hilton, D.R., Mutlu, H., 2002. Helium isotope variations in Turkey: relationship to tectonics, volcanism and recent seismic activities. *Chemical Geology* 187, 129–142.
- Hempton, M.R., Dewey, J.F., Saroglu, F., 1981. The East Anatolian transform fault: along strike variations in geometry and behavior. *Transactions American Geophysical Union EOS* 62, 393.
- Hilton, D.R., Gronvold, K., Sveinbjornsdottir, A.E., Hammerschmidt, K., 1998. Helium isotope evidence for off-axis degassing of the Icelandic hotspot. *Chemical Geology* 149, 173–187 [http://dx.doi.org/10.1016/S0009-2541\(98\)00044-8](http://dx.doi.org/10.1016/S0009-2541(98)00044-8).
- Italiano, F., Nuccio, P.M., 1991. Geochemical investigations of submarine exhalations to the East of Panarea, Aeolian Islands, Italy. *Journal of Volcanology and Geothermal Research* 46, 125–141.
- Italiano, F., Martelli, M., Martinelli, G., Nuccio, P.M., 2000. Geochemical evidence of melt intrusions along lithospheric faults of the Southern Apennines, Italy: geodynamic and seismogenic implications. *Journal of Geophysical Research* 105 (B6), 13569–13578.
- Italiano, F., Bonfanti, P., Ditta, M., Petrini, R., Slejko, F., 2009. Helium and carbon isotopes in the dissolved gases of Friuli region (NE Italy): geochemical evidence of  $CO_2$  production and degassing over a seismically active area. *Chemical Geology* 266, 76–85 <http://dx.doi.org/10.1016/j.chemgeo.2009.05.022>.
- Jackson, J., McKenzie, D.P., 1984. Active tectonics of the Alpine–Himalayan Belt between western Turkey and Pakistan. *Geophysical Journal of the Royal Astronomical Society* 77, 185–264.
- Javoy, M., Pineau, F., Delorme, H., 1986. Carbon and nitrogen isotopes in the mantle. *Chemical Geology* 57, 41–62.
- Keightley, W., 1975. Destructive Earthquakes in Burdur and Bingol, Turkey, May 1971. Committee on Natural Disaster, National Academy of Sciences. National Science Foundation (U.S.), Washington, D.C.
- Keskin, M., 2003. Magma generation by slab steepening and break off beneath a subduction-accretion complex: an alternative model for collision-related volcanism in Eastern Anatolia, Turkey. *Geophysical Research Letters* 30 (24), 8046–8049.
- Keskin, M., 2005. Domal Uplift and Volcanism in a Collision Zone Without a Mantle Plume: Evidence from Eastern Anatolia. <http://www.mantleplumes.org>.
- Keskin, M., Pearce, J.A., Kempton, P.D., Greenwood, P., 2006. Magma–crust interactions and magma plumbing in a post collisional setting: geochemical evidence from the Erzurum–Kars volcanic plateau, eastern Turkey. In: Dilek, Y., Pavlides, S. (Eds.), *Post Collisional Tectonics and Magmatism in the Mediterranean Region and Asia: Geological Society of America Special Paper*, 409, pp. 475–505.

- Kipfer, R., Aeschbach-Hertig, W., Baur, H., Hofer, M., Imboden, D.M., Signer, P., 1994. Injection of mantle-type helium into Lake Van (Turkey): the clue for quantifying deep water renewal. *Earth and Planetary Science Letters* 125, 357–370.
- Kissin, I.G., Pakhomov, S.I., 1967. The possibility of carbon dioxide generation at depth at moderately low temperature. *Doklady Akademii Nauk SSSR* 174, 451–454.
- Kocycigit, A., Beyhan, A., 1998. A new intracontinental transcurrent structure: the Central Anatolian Fault Zone, Turkey. *Tectonophysics* 284, 317–336.
- Kozlu, H., 1987. Misis–Andırın dolayımın stratigrafisi ve yapısal evrimi. Proceedings of the 7th Biannual Petroleum Congress of Turkey, Ankara. UCTEA Chamber of Petroleum Engineers, Turkish Association of Petroleum Geologists, Ankara, Turkey, pp. 104–116 (in Turkish).
- Manning, C.E., Ingebritsen, S.E., 1999. Permeability of the continental crust: implications of geothermal data and metamorphic systems. *Reviews of Geophysics* 37, 127–150.
- Martel, D.J., Deak, J., Dovenyi, F., Horvath, R.K., O'Nions, E.R., Oxburg, L., Stegena, L., Stute, M., 1989. Leakage of helium from the Pannonian basin. *Nature* 342, 908–912.
- Marty, B., Jambon, A., 1987.  $C^{13}He$  in volatile fluxes from the solid Earth: implications for carbon geodynamics. *Earth and Planetary Science Letters* 83, 16–26.
- Marty, B., O'Nions, R.K., Oxburgh, E.R., Martel, D., Lombardi, S., 1992. Helium isotopes in Alpine regions. *Tectonophysics* 206 (1–2), 71–78.
- Muehlberger, W.B., Gordon, M.B., 1987. Observations on the complexity of the East Anatolian fault, Turkey. *Journal of Structural Geology* 9 (7), 899–903.
- Mutlu, H., Güleç, N., Hilton, D.R., 2008. Helium–carbon relationships in geothermal fluids of western Anatolia, Turkey. *Chemical Geology* 247, 305–321.
- Mutlu, H., Güleç, N., Hilton, D.R., Aydın, H., Halldórsson, S.A., 2012. Spatial variations in gas and stable isotope compositions of thermal fluids around Lake Van: implications for crust–mantle dynamics in eastern Turkey. *Chemical Geology* 300–301 (2012), 165–176.
- Nagao, K., Matsuda, J.I., Kita, I., Ercan, T., 1989. Noble gas and carbon isotopic compositions in Quaternary volcanic area in Turkey. *Bulletin Geomorphology* 17, 101–110.
- O'Nions, R.K., Oxburgh, E.R., 1983. Heat and helium in the Earth. *Nature* 306, 429–431 <http://dx.doi.org/10.1038/306429a0>.
- O'Nions, R.K., Oxburgh, E.R., 1988. Helium, volatile fluxes and the development of the continental crust. *Earth and Planetary Science Letters* 90, 315–331.
- Okay, I.A., Kaslılar-Ozcan, A., Imren, C., Boztepe-Güney, A., Demirbag, E., Kucsu, I., 2000. Active faults and evolving strike-slip basins in the Marmara Sea, northwest Turkey: a multichannel seismic reflection study. *Tectonophysics* 321, 189–218.
- Öztekın Okan, Ö., Çetindağ, B., 2005. Hydrogeochemical and isotopic investigation of the Kolan Geothermal Field, Southeastern Turkey. *Environmental Geology* 48, 179–188.
- Paonita, A., Martelli, M., 2007. A new view of the He–Ar–CO<sub>2</sub> degassing at mid-ocean ridges: homogeneous composition of magmas from the upper mantle. *Geochemistry et Cosmochimica Acta* 71, 1747–1763.
- Pearce, J.A., Bender, J.F., De Long, S.E., Kidd, W.S.F., Low, P.J., Guner, Y., Saroglu, F., Yilmaz, Y., Moorbath, S., Mitchell, J.G., 1990. Genesis of collision volcanism in Eastern Anatolia, Turkey. *Journal of Volcanology and Geothermal Research* 44, 189–229.
- Perincek, D., Cemen, I., 1990. The structural relationship between the East Anatolian and Dead Sea fault zones in southeastern Turkey. *Tectonophysics* 172, 331–340.
- Perincek, D., Gunay, Y., Kozlu, H., 1987. New observations on strike-slip faults in east and southeast Anatolia. 7th Petroleum Congress of Turkey, UCTEA Chamber of Petroleum Engineers, Turkish Association of Petroleum Geologists, Ankara, pp. 89–103.
- Pfister, M., Balderer, W., Greber, E., Kahle, H.G., Mayer-Rosa, D., Mueller, S., Rybach, L., Schindler, C., Sellami, S., Straub, C., 1997. Synthesis of the Marmara poly-project. In: Schindler, C., Pfister, M. (Eds.), *Tectonics of Northwestern Anatolia—the Marmara Poly-project*. Vdf Hochschulverlag an der ETH, Zurich, pp. 539–565.
- Polyak, B.G., Tolstikhin, I.N., 1985. Isotopic composition of the Earth's helium and the problem of tectogenesis. *Chemical Geology* 52, 9–33.
- Reilinger, R., et al., 2006. GPS constraints on continental deformation in the Africa–Arabia–Eurasia continental collision zone and implications for the dynamics of plate interactions. *Journal of Geophysical Research* 111, B05411 <http://dx.doi.org/10.1029/2005JB004051>.
- Sano, Y., Marty, B., 1995. Origin of carbon in fumarolic gas from island arc. *Chemical Geology* 119, 265–274 [http://dx.doi.org/10.1016/0009-2541\(94\)00097-R](http://dx.doi.org/10.1016/0009-2541(94)00097-R).
- Saroglu, F., Emre, O., Kucsu, I., 1992. The East Anatolian fault zone of Turkey. *Annales Tectonicae* 99–125 (Special Issue-Supplement to Volume VI).
- Sengör, A.M.C., Gorur, N., Saroglu, F., 1985. Strike slip faulting and related basin formations in zones of tectonic escape: Turkey as a case study. In: Biddle, K.T., Christie-Blick, N. (Eds.), *Strike-slip faulting and basin formation*. : Special Publication No. 37. Society of Economic Paleontologists and Mineralogists, Tulsa, Oklahoma, pp. 227–264.
- Sengör, A.M.C., Ozeren, S., Genc, T., Zor, E., 2003. East Anatolian high plateau as a mantle-supported, north–south shortened domal structure. *Geophysical Research Letters* 30, 8045.
- Sengör, A.M. Celâl, Ozeren, M.S., Keskin, M., Sakıncı, M., Ozbakir, A.D., Kayan, I., 2008. Eastern Turkish high plateau as a small Turkish-type orogen: implications for post-collisional crust-forming processes in Turkish-type orogens. *Earth-Science Reviews* 90, 1–48.
- Seymen, I., Aydın, A., 1972. Bingöl deprem fayı ve bunun Kuzey Anadolu fay zonu ile ilişkisi (The Bingöl earthquake fault and its relation to the North Anatolian fault zone). *Bulletin of the Mineral Research and Exploratory Institute of Turkey* 79, 1–8.
- Stone, J.O.H.S., 1986. Helium isotopic tracing of fluids in the lithosphere. Unpublished PhD Thesis, University of Cambridge, UK.
- Sugisaki, R., Taki, K., 1987. Simplified analyses of He, Ne, and Ar dissolved in natural waters. *Geochemical Journal* 21, 23–27.
- Tarhan, N., 1991. Hınıs–Varto–Karlöva (Erzurum–Muş–Bingöl) Dolayındaki Neojen Volkanitlerinin Jeolojisi ve Petrolojisi. *MTA Dergisi* 113, 1–15 (in Turkish).
- Taşkıran, L., 2006. Hydrogeochemical investigation of thermal spring waters in Southwest of Tekman (Erzurum). Master Thesis. Osmangazi University Institute of Science, 61 p.
- Tchalenko, J.S., 1977. A reconnaissance of seismicity and tectonics at the northern border of the Arabian plate (Lake Van region). *Reviews of Geographical Physics Geological Dynamics* 19, 189–208.
- Topuz, G., Altherr, R., Kalt, A., Satör, M., Werner, O., Schwarz, W.H., 2004. Aluminous granulites from the Pulur complex, NE Turkey: a case of partial melting, efficient melt extraction and crystallization. *Lithos* 72, 183–207.
- U.S. National Committee for Rock Mechanics, 1996. *Rock Fractures and Fluid Flow*. 551 pp. National Academy Press, Washington.
- Wakita, H., Fujii, N., Matsuo, S., Notsu, K., Nagao, K., Takaoka, N., 1978. “Helium spots”: caused by a diapiric magma from the upper mantle. *Science* 200, 430–432.
- Weiss, R.F., 1971. Solubility of helium and neon in water and seawater. *Journal of Chemical & Engineering Data* 16, 235–241.
- Westaway, R., 1994. Present-day kinematics of the Middle East and eastern Mediterranean. *Journal of Geophysical Research* 99 (B6), 12071–12090.
- Yilmaz, Y., Guner, Y., Saroglu, F., 1998. Geology of the quaternary volcanic centres of the east Anatolia. *Journal of Volcanology and Geothermal Research* 85 (1–4), 173–210.